Electronic Supplementary Information

Infrared characterization of the products and the rate coefficient of the reaction between Criegee intermediate CH₂OO and HCl

Wei-Che Liang,[a] Pei-Ling Luo,*[ab] and Yuan-Pern Lee*[abc]

[a] *Department of Applied Chemistry and Institute of Molecular Science, National Yang Ming Chiao Tung University, Hsinchu 300093, Taiwan.*

[b] *Institute of Atomic and Molecular Sciences, Academia Sinica, Taipei 106319, Taiwan.*

[c] *Center for Emergent Functional Matter Science, National Chiao Tung University, Hsinchu 300093, Taiwan.*

E-mail: plluo@gate.sinica.edu.tw (P.-L. Luo)
E-mail: yplee@nycu.edu.tw (Y.-P. Lee)

ESI includes 1 note, 6 tables, and 10 figures.

Note S1. Simulation of Bands A$_2$−A$_4$ of *gauche*-CMHP

With the PGOPHER program,[1] we simulated the fundamental band of each vibrational mode by using rotational parameters A'', B'', and C'', ratios of rotational parameters A'/A'', B'/B'', and C'/C'' and $a/b/c$ type ratios of each mode predicted with the B3LYP/aug-cc-pVTZ-pp method, as listed in Tables S3 and S4 (ESI†), J_{max} = 200, T = 298 K, and a Gaussian width 0.32 cm^{-1} (corresponding to the instrument resolution 0.25 cm^{-1} after apodization). The projections of the dipole derivatives for each vibrational mode of *gauche*-CMHP onto rotational axes a, b and c determine the weighting of bands of types a, b, and c in each vibrational absorption band. For an improved simulation, we employed ratios of calculated rotational parameters A'/A'', B'/B'', and C'/C'' and experimental values of A'', B'', and C'' derived from microwave experiments by Cabezas and Endo,[2] Simulated $a/b/c$-type spectra and the resultant rotational contours for v_5, v_6, v_8, and v_{10} of *gauche*-^{35}Cl-CMHP are shown in Fig. S4 (ESI†).

Because information was lacking, we assumed that the rotational contours and the IR intensities of the hot bands are the same as the fundamental band. The contours of the hot bands were consequently derived from the fundamental band with intensities scaled according to a Boltzmann distribution and positions shifted according to anharmonicity; the shifts depend on the difference in transition wavenumbers between the fundamental band and the hot bands. We calculated, as initial estimates, the Boltzmann distributions of the excited states of the low-energy modes according to the predicted anharmonic vibrational energies; the shifts among hot bands in a series were initially assumed to be constant. For *gauche*-CMHP, the two least-energy vibrational modes v_{14} and v_{15} were considered; their v = 1 states have energies 150 and 284 cm^{-1}, respectively, above the ground state. A least-squares fit was performed on systematically varying these parameters within limited ranges in position (≤ 5 cm^{-1}) and intensities (within ±10%) for each band. It should be noted that the decomposition of observed spectra to several series of transitions is not unique; such decomposition is

only used as an attempt to explain that the observed broad rotational contours might be due to contributions of the hot bands and isotopic species.

For band A$_2$, contributions from the fundamental band ν_8, 8_0^1, hot bands associated with ν_{15}, $8_0^1 15_a^a$ with $a = 1-4$, and ν_{14}, $8_0^1 14_a^a$ with $a = 1-2$, were considered, as shown in Fig. S7(b), ESI†. Furthermore, *gauche*-^{37}Cl-CMHP also contribute, with 8_0^1, $8_0^1 15_a^a$ with $a = 1-3$, and $8_0^1 14_1^1$; a red shift of 1.2 cm^{-1} from *gauche*-^{35}Cl-CMHP for 8_0^1 was predicted from calculation, as shown in Fig. S7(c), ESI†. For the simulation of bands A$_3$ and A$_4$, we did not include contributions of *gauche*-^{37}Cl-CMHP for simplicity.

Table S1 Harmonic and anharmonic vibrational wavenumbers (cm^{-1}) and IR intensities (km mol^{-1}) of *gauche*-CMHP and *anti*-CMHP calculated with B3LYP/aug-cc-pVTZ

Mode	*gauche*-CMHP		*anti*-CMHP	
	Harmonic	Anharmonic	Harmonic	Anharmonic
ν_1	3717 (36)	3539	3748 (56)	3565
ν_2	3170 (1)	3022	3125 (10)	2978
ν_3	3091 (9)	2971	3059 (21)	2885
ν_4	1456 (2)	1417	1511 (3)	1472
ν_5	1391 (58)	1353	1371 (16)	1361
ν_6	1322 (39)	1292	1340 (73)	1291
ν_7	1267 (9)	1236	1209 (3)	1182
ν_8	1079 (87)	1047	1050 (44)	1018
ν_9	996 (1)	977	1004 (0)	992
ν_{10}	878 (20)	855	921 (9)	897
ν_{11}	664 (131)	655	781 (90)	761
ν_{12}	494 (23)	484	398 (1)	392
ν_{13}	366 (7)	359	271 (7)	317
ν_{14}	260 (107)	284	240 (106)	137
ν_{15}	143 (19)	150	93 (4)	85

Table S2 Harmonic and anharmonic vibrational wavenumbers (cm^{-1}) and IR intensities (km mol^{-1}) of *gauche*-MCP and CH$_2$ClO calculated with B3LYP/aug-cc-pVTZ

Mode	*gauche*-MCP		CH$_2$ClO	
	Harmonic	Anharmonic	Harmonic	Anharmonic
ν_1	3128 (7)	2983	2942 (4)	2731
ν_2	3105 (19)	2960	2914 (38)	2723
ν_3	3028 (20)	2949	1308 (57)	1312
ν_4	1500 (13)	1498	1226 (10)	1166
ν_5	1467 (9)	1425	1136 (48)	1115
ν_6	1445 (2)	1431	1035 (0)	1008
ν_7	1202 (3)	1173	648 (160)	627
ν_8	1167 (2)	1139	647 (2)	752
ν_9	986 (33)	952	381 (5)	371
ν_{10}	845 (23)	828		
ν_{11}	600 (44)	583		
ν_{12}	477 (1)	470		
ν_{13}	349 (8)	346		
ν_{14}	201 (2)	180		
ν_{15}	140 (2)	137		

Table S3 Rotational parameters (in cm^{-1}) of the ground state and vibrationally excited states ($v = 1$) of *gauche*-CMHP, *anti*-CMHP, and *gauche*-MCP predicted with the B3LYP/aug-cc-pVTZ method

Mode	*gauche*-CMHP			*anti*-CMHP			*gauche*-MCP		
	A'	B'	C'	A'	B'	C'	A'	B'	C'
ν_1	0.486	0.114	0.099	1.178	0.087	0.083	0.569	0.114	0.103
ν_2	0.487	0.114	0.099	1.180	0.087	0.083	0.568	0.114	0.103
ν_3	0.487	0.114	0.099	1.179	0.087	0.083	0.568	0.114	0.103
ν_4	0.488	0.113	0.099	1.177	0.087	0.083	0.570	0.114	0.103
ν_5	0.488	0.113	0.099	1.181	0.087	0.082	0.577	0.114	0.103
ν_6	0.487	0.113	0.099	1.179	0.087	0.082	0.556	0.114	0.103
ν_7	0.486	0.114	0.099	1.176	0.087	0.083	0.569	0.114	0.103
ν_8	0.487	0.113	0.099	1.184	0.086	0.082	0.564	0.114	0.103
ν_9	0.486	0.113	0.099	1.171	0.086	0.082	0.564	0.113	0.103
ν_{10}	0.487	0.113	0.099	1.179	0.086	0.082	0.568	0.113	0.103
ν_{11}	0.488	0.113	0.099	1.177	0.086	0.082	0.565	0.113	0.103
ν_{12}	0.487	0.113	0.099	1.185	0.086	0.082	0.569	0.113	0.103
ν_{13}	0.488	0.113	0.099	1.208	0.087	0.082	0.567	0.113	0.103
ν_{14}	0.488	0.113	0.099	1.186	0.087	0.082	0.570	0.113	0.103
ν_{15}	0.493	0.113	0.099	1.145	0.087	0.083	0.577	0.113	0.103
	A''	B''	C''	A''	B''	C''	A''	B''	C''
$v = 0$	0.488	0.113	0.099	1.181	0.087	0.083	0.568	0.114	0.103
scaled[a]	0.479	0.120	0.103	1.159	0.092	0.086	0.557	0.112	0.101

[a]The rotational parameters scaled with those derived from the microwave spectrum of *gauche*-CMHP.[2]

Table S4 Ratios of *a*-, *b*-, and *c*-types of vibrational bands for each vibrational mode of *gauche*-CMHP, *anti*-CMHP, and *gauche*-MCP predicted with the B3LYP/aug-cc-pVTZ method

Mode	*gauche*-CMHP			*anti*-CMHP			*gauche*-MCP		
	a	*b*	*c*	*a*	*b*	*c*	*a*	*b*	*c*
ν_1	0.00	0.80	0.20	0.53	0.08	0.39	0.01	0.00	0.99
ν_2	0.25	0.12	0.63	0.00	0.00	0.99	0.51	0.25	0.24
ν_3	0.04	0.62	0.34	0.00	0.96	0.03	0.39	0.43	0.18
ν_4	0.02	0.12	0.87	0.85	0.14	0.01	0.82	0.00	0.18
ν_5	0.31	0.64	0.05	0.97	0.03	0.01	0.13	0.63	0.24
ν_6	0.90	0.06	0.04	0.87	0.12	0.00	0.59	0.40	0.01
ν_7	0.59	0.13	0.28	0.25	0.04	0.71	0.17	0.40	0.43
ν_8	0.92	0.01	0.07	0.43	0.57	0.00	0.44	0.36	0.20
ν_9	0.08	0.50	0.42	0.42	0.12	0.47	0.66	0.19	0.15
ν_{10}	0.87	0.04	0.09	0.75	0.24	0.01	0.66	0.31	0.03
ν_{11}	0.82	0.17	0.01	0.98	0.02	0.00	0.95	0.05	0.00
ν_{12}	1.00	0.00	0.00	0.68	0.28	0.04	0.06	0.92	0.02
ν_{13}	0.59	0.30	0.11	0.41	0.51	0.08	0.89	0.09	0.02
ν_{14}	0.45	0.00	0.55	0.12	0.67	0.21	0.67	0.18	0.15
ν_{15}	0.79	0.20	0.01	0.48	0.49	0.04	0.44	0.56	0.00

Table S5 Summary of experimental conditions and fitted rate coefficients

Set[a]	Expt.	$[CH_2I_2]_0$ /mTorr	$[CH_2I]_0$ /10^{13} [b]	$[CH_2OO]_0$ /10^{13} [b]	$[HCl]_0$ /10^{14} [b]	$[O_2]$ /Torr	k^I, exponential fit /10^3 s^{-1}	k^I, model fit /10^3 s^{-1}
1	1	10.6	1.38	1.10	0.91	5.2	7.2	4.7
	2	10.6	1.38	1.10	6.22	5.2	34.0	29.5
	3	10.6	1.38	1.10	12.46	5.2	66.2	60.8
	4	10.6	1.38	1.10	1.53	5.2	10.9	7.6
	5	10.6	1.38	1.10	3.09	5.2	18.1	15.1
2	6	10.0	1.30	1.03	4.68	5.2	26.0	22.6
	7	10.0	1.30	1.03	9.33	5.2	49.9	45.5
	8	10.0	1.30	1.03	15.57	5.2	79.3	73.0
	9	10.0	1.30	1.03	7.78	5.2	42.2	38.2
3	10	16.6	2.15	1.70	12.41	8.2	65.1	58.4
	11	16.6	2.15	1.70	2.50	8.2	16.0	12.5
	12	16.6	2.15	1.70	4.94	8.2	29.0	25.4
	13	16.6	2.15	1.70	19.88	8.2	103.2	97.4
4	14	16.1	2.09	1.66	1.45	8.2	10.3	6.9
	15	16.1	2.09	1.66	7.49	8.2	40.1	36.9
	16	16.1	2.09	1.66	14.92	8.2	77.2	72.5
	17	16.1	2.09	1.66	9.94	8.2	54.9	48.8

[a] For all experiments, a CH_2OO line at 896.876 cm^{-1} was probed and the photolysis beam has fluence 20 mJ cm^{-2}. [b] in unit of molecule cm^{-3}.

Table S6 Kinetic model and rate coefficients employed in the fitting for $CH_2OO + HCl$

	Reaction	Rate coefficient [a]	Ref.
k_{1a} [b]	$CH_2I + O_2 \rightarrow CH_2OO + I$	$\{1 - 0.47/(1+3.2\times10^{-18}\,[M])\}\times1.6\times10^{-12}$ $/(1+1.1\times10^{-19}\,[M])$	3
k_{1b} [b]	$CH_2I + O_2 \rightarrow CH_2IOO$	$1.6\times10^{-12} - 1.6\times10^{-12}\,/(1+1.1\times10^{-19}\,[M])$	3
k_{1c} [b]	$CH_2I + O_2 \rightarrow CH_2O + IO$	4.0×10^{-13}	4
k_{1d} [b]	$CH_2I + O_2 \rightarrow$ other products	$1.6\times10^{-12} - k_{1a} - k_{1b} - k_{1c}$	3
k_{2a}	$CH_2OO + I \rightarrow CH_2I + O_2$	$55\times1.6\times10^{-12}\,/(1+1.1\times10^{-19}\,[M])$	3
k_{2b}	$CH_2OO + I \rightarrow CH_2IOO$	$55\times\{1.6\times10^{-12} - 1.6\times10^{-12}\,/(1+1.1\times10^{-19}\,[M])\}$	3
k_{2c}	$CH_2OO + I \rightarrow CH_2O + IO$	9.0×10^{-12}	3
k_3	$CH_2OO + CH_2I \rightarrow C_2H_4I + O_2$	6.3×10^{-11}	5
k_{self}	$CH_2OO + CH_2OO \rightarrow 2CH_2O + O_2$	9.2×10^{-11}	6
k_5	$IO + IO \rightarrow I_2 + O_2$	9.9×10^{-11}	7
k_6	$CH_2IOO + I \rightarrow CH_2IO + IO$	3.5×10^{-11}	8
k_7	$CH_2IOO + CH_2IOO \rightarrow 2CH_2IO + O_2$	9.0×10^{-11}	8
k_8	$CH_2IO \rightarrow CH_2O + I$	$10^6\,s^{-1}$	8
k_9	$CH_2OO + HCl \rightarrow$ products	$k^I = k_9\times[HCl]_0$, fitted	

[a] Rate coefficient in cm^3 molecule^{-1} s^{-1}, unless specified, [M] in molecule cm^{-3}. [b] $k_{1a} + k_{1b} + k_{1c} + k_{1d}$ = 1.6×10^{-12} cm^3 molecule^{-1} s^{-1}.
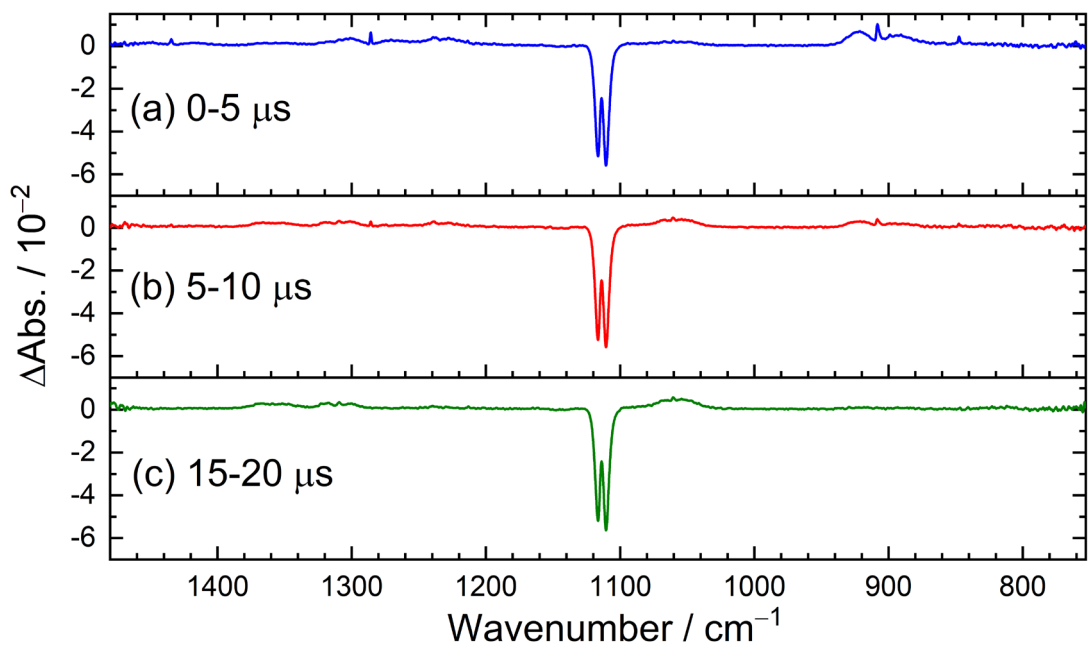
Fig. S1 Difference spectra at resolution 1.0 cm^{-1} recorded upon photolysis at 308 nm of a flowing mixture of CH_2I_2/HCl/N_2/O_2 (0.07/0.04/54.0/46.0, P_T = 100.1 Torr, 298 K). (a)–(c) Spectra recorded 0–5, 5–10, and 15–20 μs after irradiation, respectively.
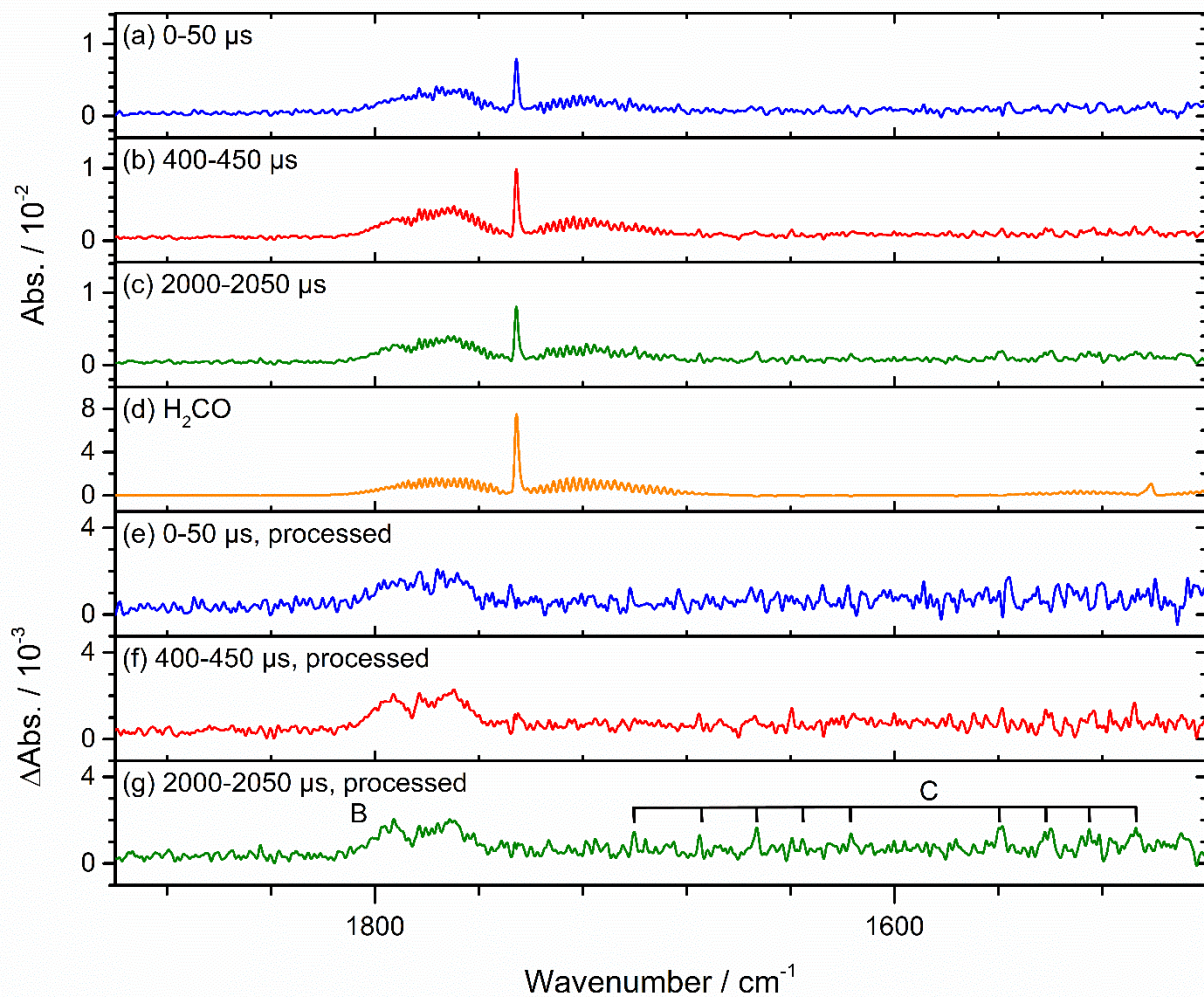
**Fig. S2** Difference absorbance spectra at resolution 1.0 cm^{-1} recorded upon photolysis at 308 nm of a flowing mixture of CH$_2$I$_2$/HCl/N$_2$/O$_2$ (0.08/0.04/51.7/49.2, P_T = 101.0 Torr, 298 K). (a)–(c) Spectra recorded 0–50, 400–450, and 2000–2050 μs after irradiation, respectively. (d) IR spectrum of H$_2$CO. (e)–(g) Processed spectra of (a)–(c) with absorption of H$_2$CO subtracted; features B and lines of group C are indicated.
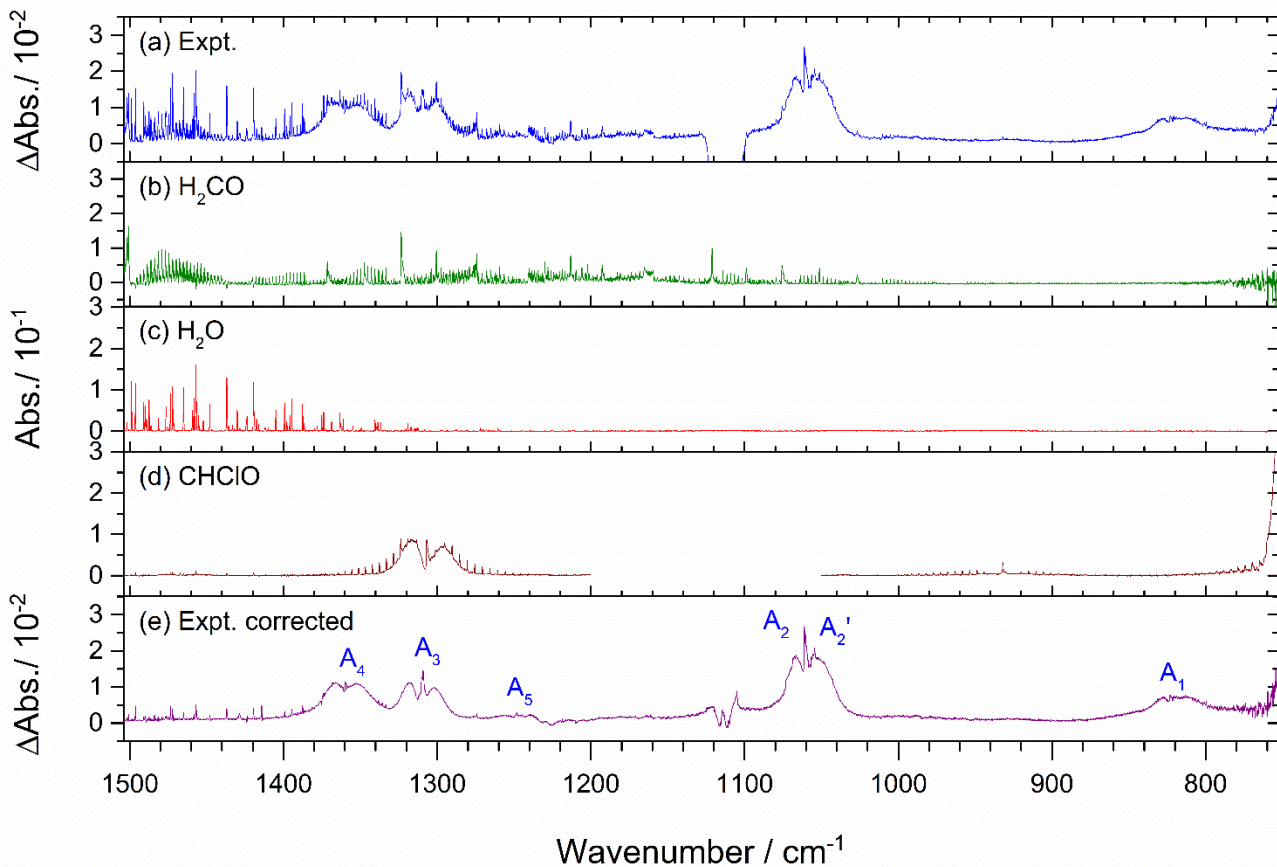
Fig. S3 (a) Difference absorbance spectrum recorded upon 308-nm photolysis of a flowing mixture of $CH_2I_2/HCl/N_2/O_2$ (0.12/0.6/54.0/46.0, P_T = 100.7 Torr) by using continuous-scan mode at resolution 0.25 cm^{-1}. (b) IR spectrum of H_2CO. (c) IR spectrum of H_2O (d) IR spectrum of CHClO. (e) Processed spectrum with absorption of H_2CO, H_2O and CHClO subtracted; features in group A are indicated.
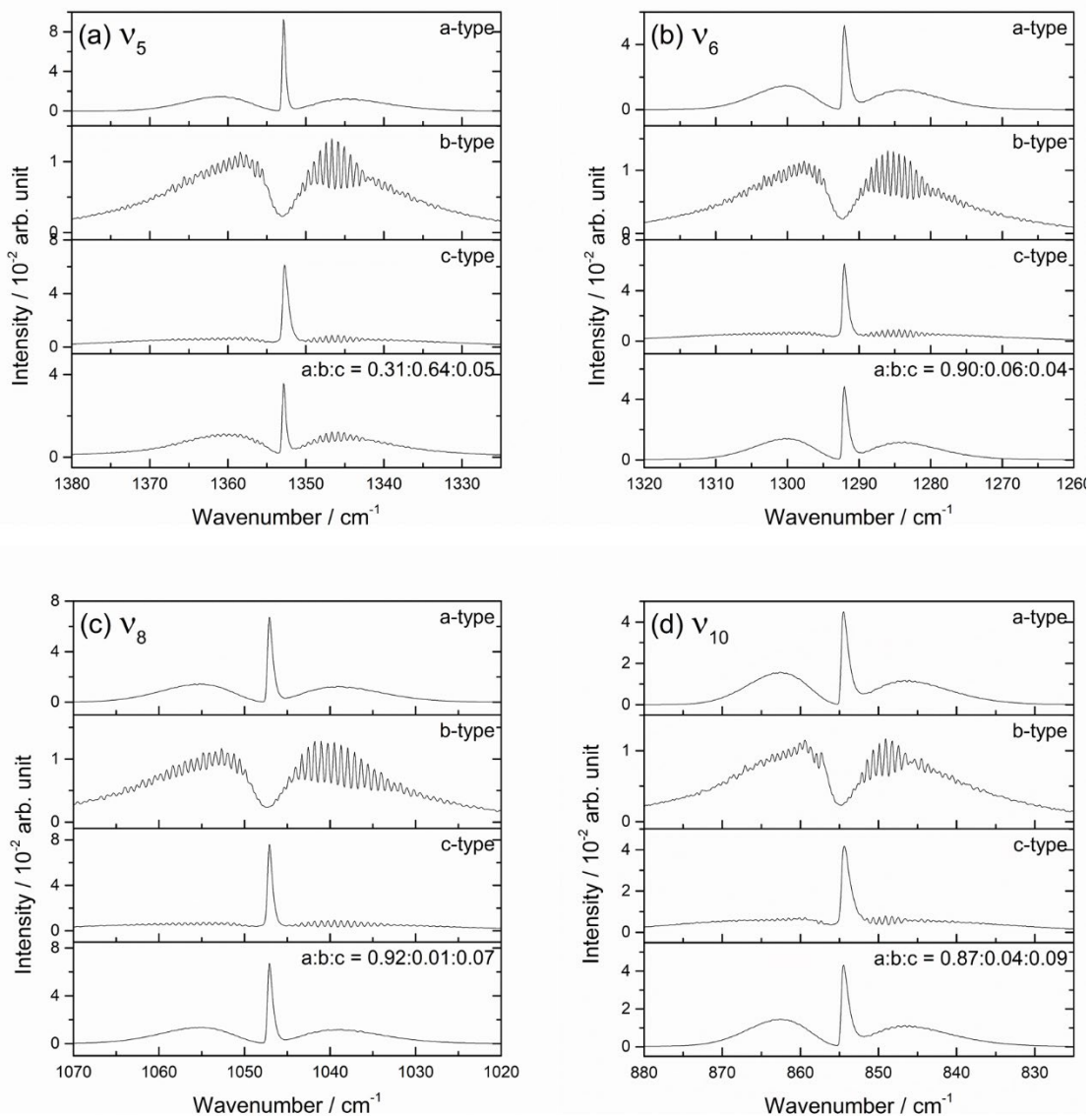
Fig. S4 Simulated rotational contours for ν_5, ν_6, ν_8 and ν_{10} modes of *gauche*-CMHP. Type *a*, type *b*, type *c*, and resultant rotational contours according to the weighting factors determined according to the projections of the predicted dipole derivatives onto axes *a*, *b* and *c* are shown.
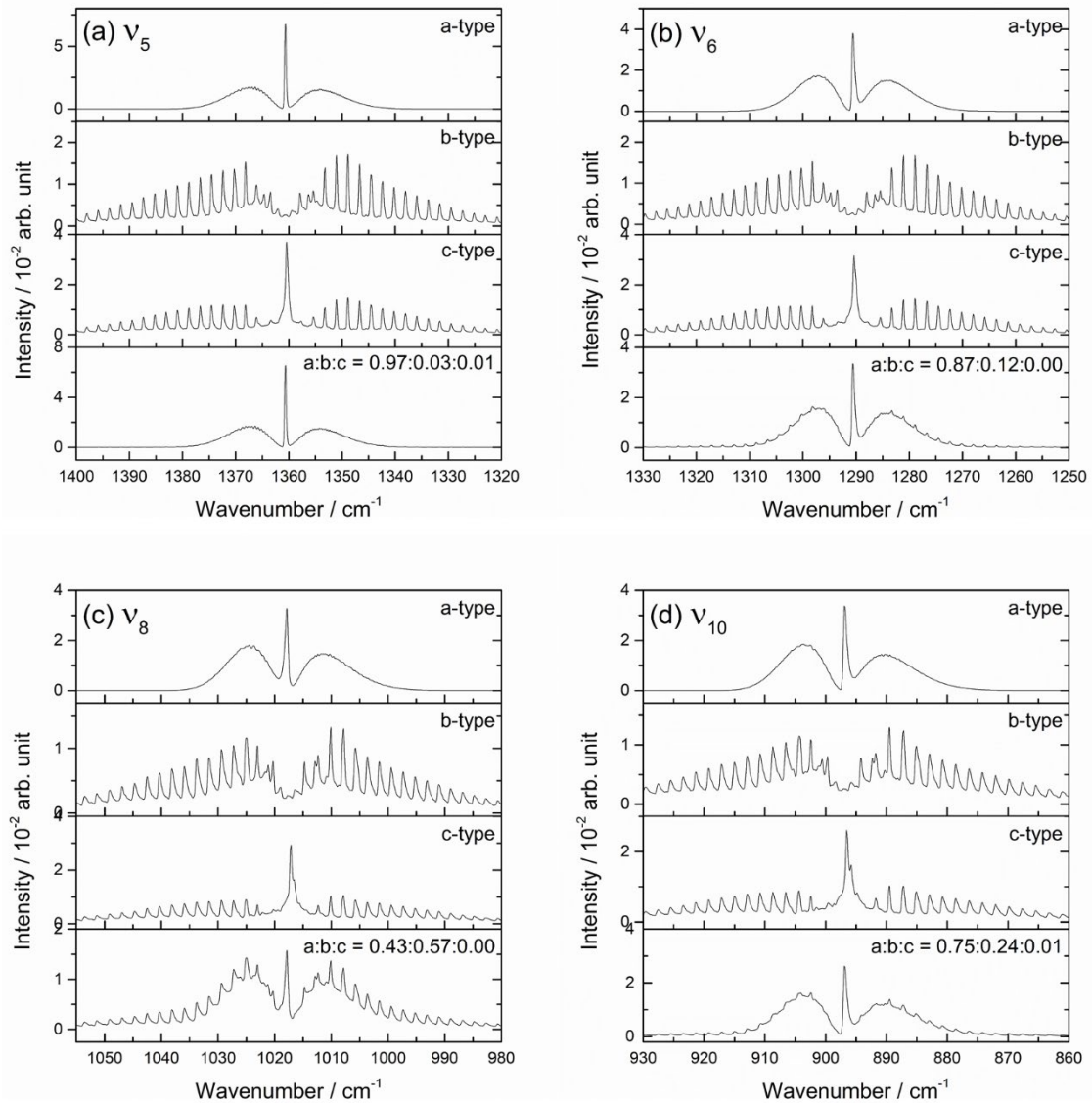
Fig. S5 Simulated rotational contours for ν_5, ν_6, ν_8 and ν_{10} modes of *anti*-CMHP. Type *a*, type *b*, type *c*, and resultant rotational contours according to the weighting factors determined according to the projections of the predicted dipole derivatives onto axes *a*, *b* and *c* are shown.
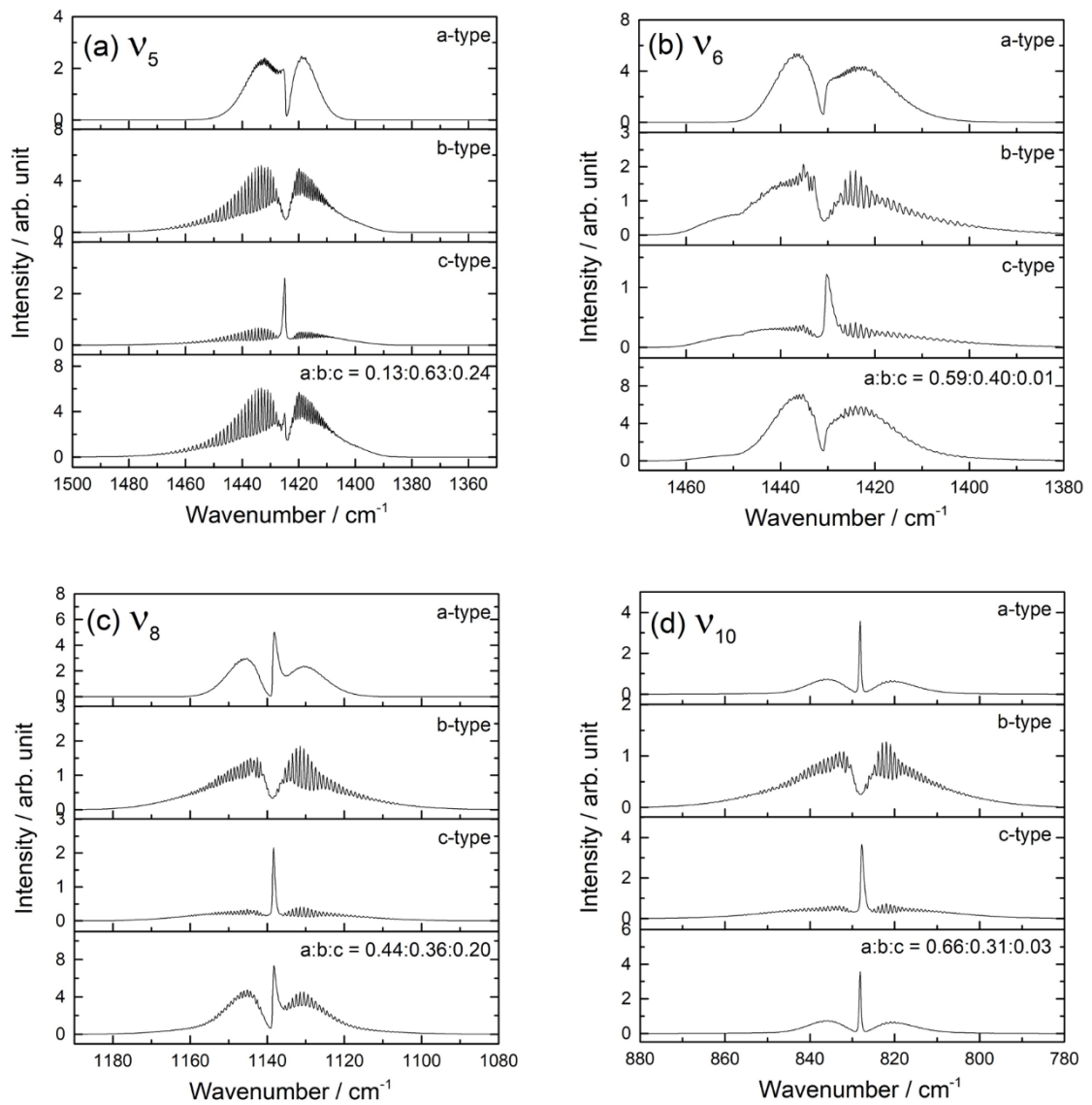
Fig. S6 Simulated rotational contours for ν$_5$, ν$_6$, ν$_8$ and ν$_{10}$ modes of *gauche*-MCP. Type *a*, type *b*, type *c*, and resultant rotational contours according to the weighting factors determined according to the projections of the predicted dipole derivatives onto axes *a*, *b* and *c* are shown.
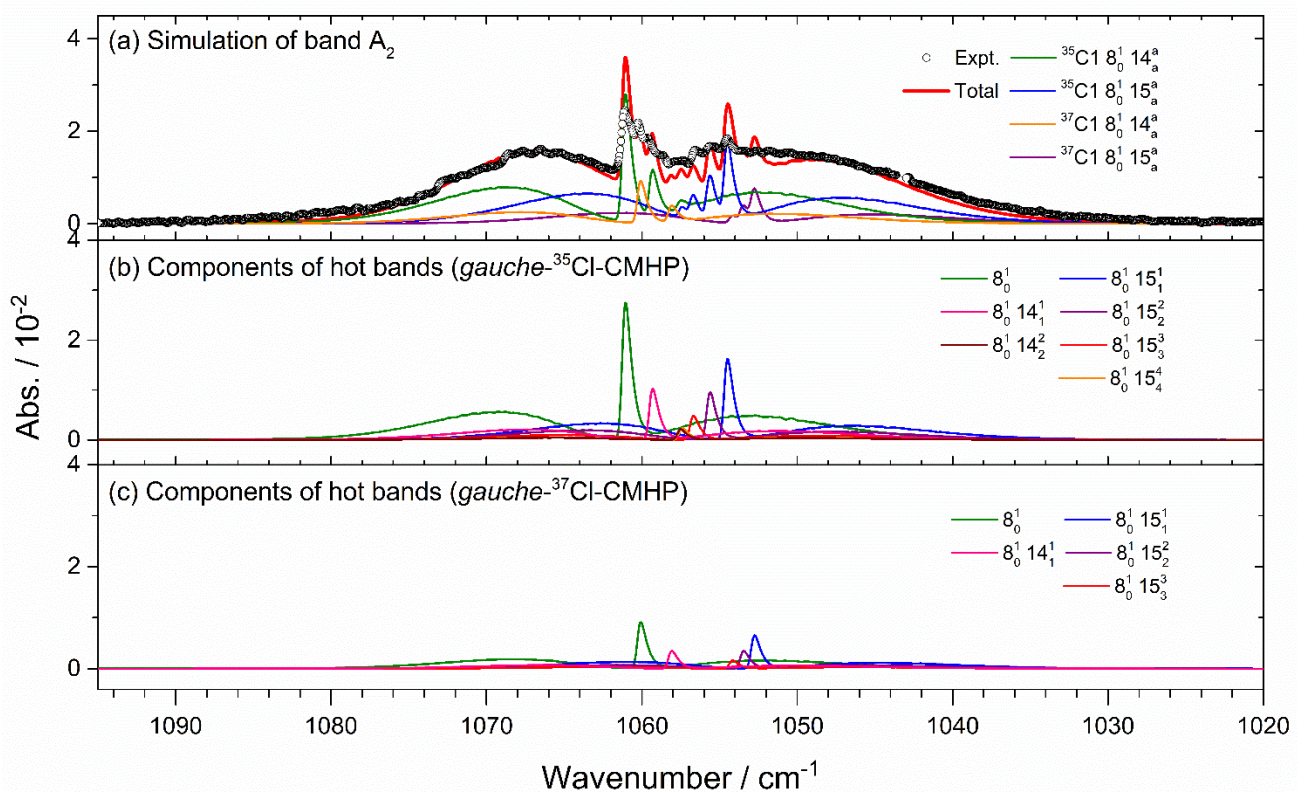
Fig. S7 Spectral simulation of bands A_2 and A_2'. (a) Comparison of experimental spectrum (open circle) with a simulated spectrum (thick red solid line); contributions from the fundamental bands (ν_8) of *gauche*-^{35}Cl-CMHP and *gauche*-^{37}Cl-CMHP and two series of hot bands are shown in thin lines (green for the fundamental band of *gauche*-^{35}Cl-CMHP and hot bands from ν_{14}, orange for the fundamental band of *gauche*-^{37}Cl-CMHP and hot bands from ν_{14}, and blue and purple for hot bands from ν_{15}). (b) Contributions of fundamental and hot bands of *gauche*-^{35}Cl-CMHP. (c) Contributions from *gauche*-^{37}CMHP. Instrumental resolution is 0.25 cm^{-1}, which corresponds to spectral width 0.32 cm^{-1} of simulation.
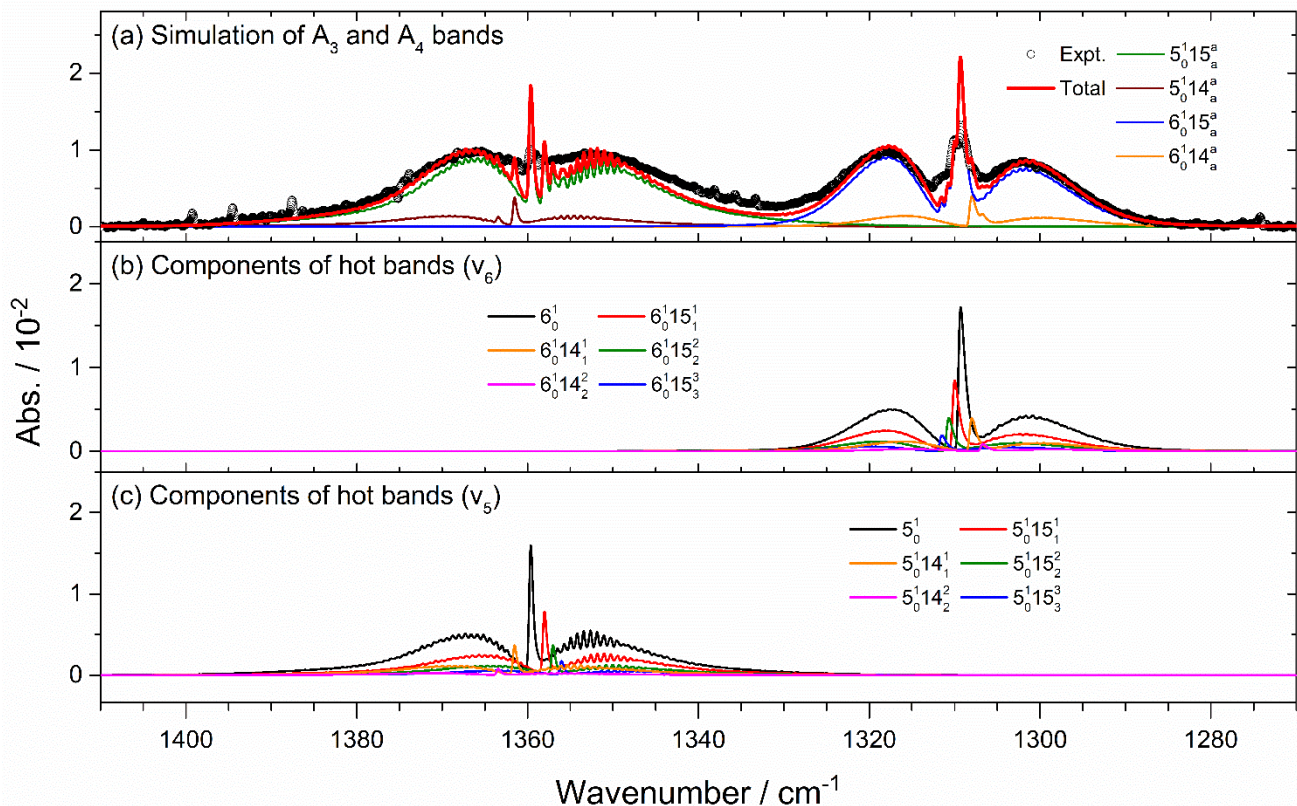
Fig. S8 Spectral simulation of the A_3 and A_4 bands. (a) Comparison of experimental spectrum (open circle) with a simulated spectrum (thick red solid line); contributions from the fundamental bands (ν_5 and ν_6) of *gauche*-^{35}Cl-CMHP and two series of hot bands are shown in thin lines (green for the fundamental band (ν_5) and hot bands from ν_{15}, blue for the fundamental band (ν_6) and hot bands from ν_{15}, and orange and purple for hot bands from ν_{14}). (b) Contributions of fundamental and hot bands of ν_6. (c) Contributions of ν_5. Instrumental resolution is 0.25 cm^{-1}, which corresponds to spectral width 0.32 cm^{-1} of simulation.
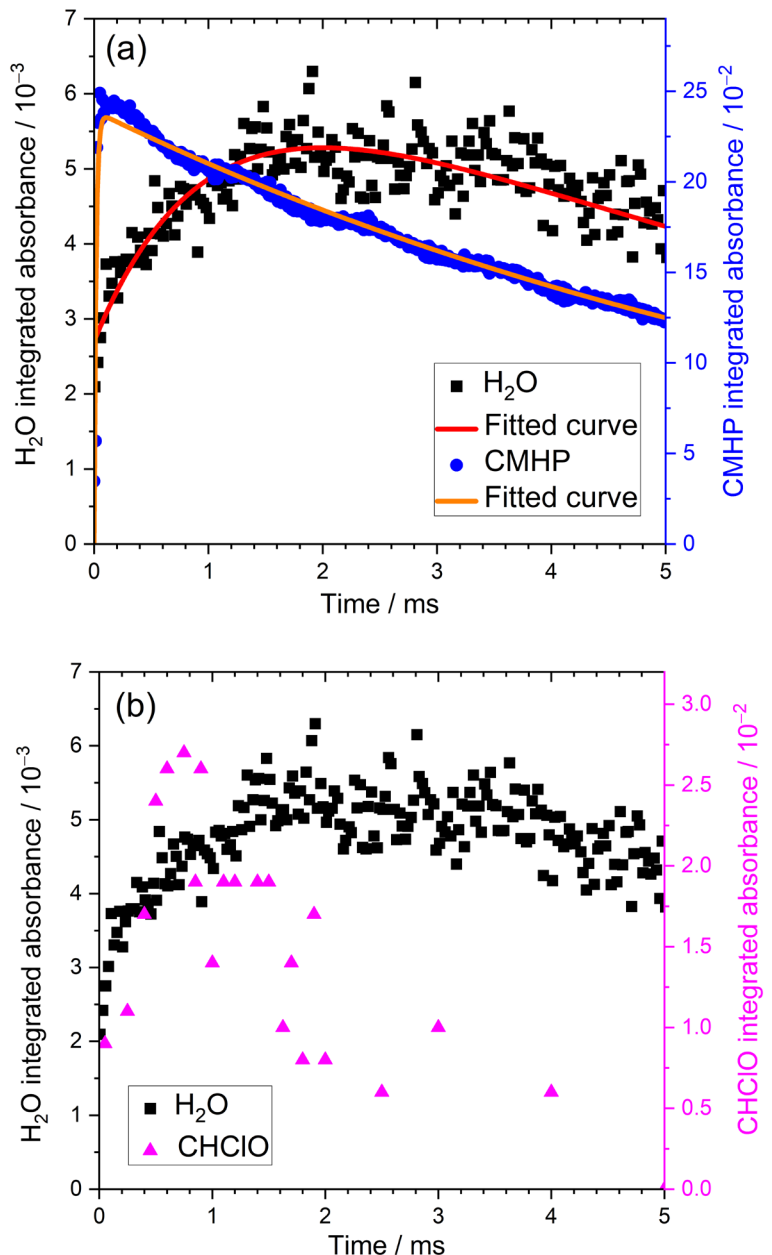
Fig. S9 Temporal profiles of *gauche*-CMHP, H_2O, and CHClO obtained on integration over regions 1030–1085, 1557–1560, and 1758–1810 cm^{-1}, respectively, of the difference spectra recorded on photolysis at 308 nm of a flowing mixture of $CH_2I_2/HCl/N_2/O_2$ (0.08/0.04/51.7/49.2, 101.0 Torr, 298 K). (a) Measured temporal profiles of CMHP (blue circles) and H_2O (black squares) with the fitted curves. (b) Comparison of the temporal profiles of H_2O (black squares) and CHClO (pink triangles; the data of CHClO have large uncertainties because of the severe interference from absorption of H_2CO.
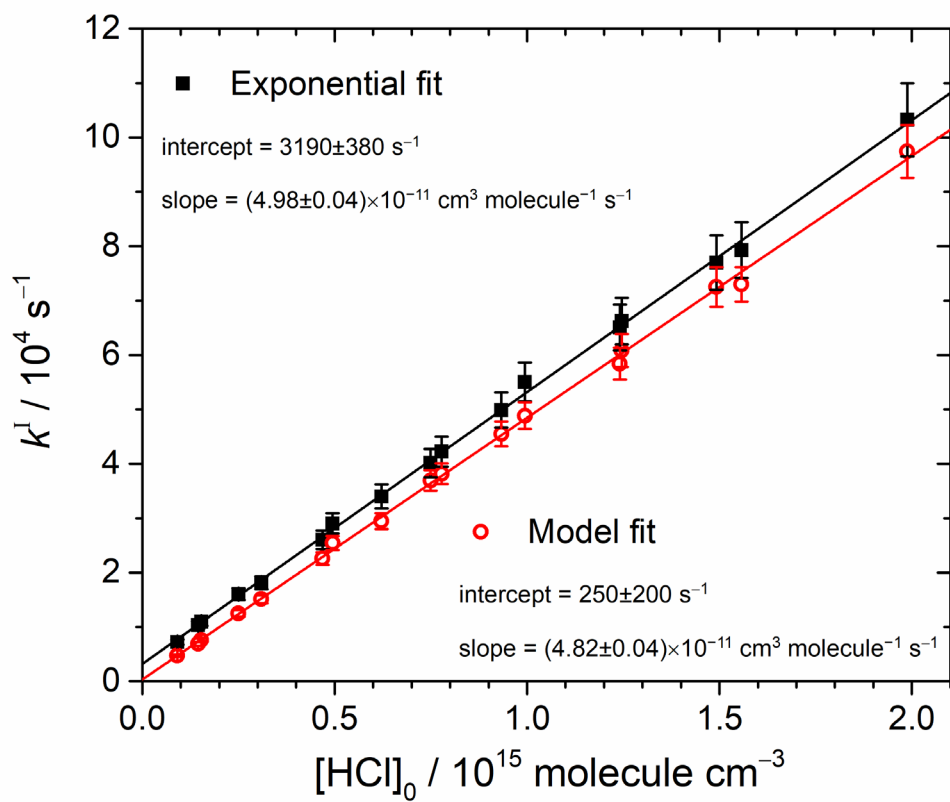
Fig. S10 Comparison of plots of k^I vs. $[HCl]_0$ derived from model fit and single-exponential fit.

References

1. C. M. Western, "PGOPHER, a Program for Simulating Rotational Structure," http://pgopher.chm.bris.ac.uk/.

2. C. Cabezas and Y. Endo, *Chem. Phys. Chem.*, 2017, **18**, 1860–1863.

3. W.-L. Ting, C.-H. Chang, Y.-F. Lee, H. Matsui, Y.-P. Lee and J. J.-M. Lin, J. Chem. Phys., 2014, **141**, 104308.

4. S. Enami, J. Ueda, M. Goto, Y. Nakano, S. Aloisio, S. Hashimoto and M. Kawasaki, J. Phys. Chem. A, 2004, **108**, 6347−6350.

5. Y.-T. Su, H.-Y. Lin, R. Putikam, H. Matsui, M. C. Lin and Y.-P. Lee, Nat. Chem., 2014, **6**, 477−483.

6. P.-L. Luo, Y. Endo and Y.-P. Lee, J. Phys. Chem. Lett., 2018, **9**, 4391–4395.

7. R. Atkinson, D. L. Baulch, R. A. Cox, J. N. Crowley, R. F. Hampson, Jr., R. G. Hynes, M. E. Jenkin, M. J. Rossi and J. Troe, Atmos. Chem. Phys., 2007, **7**, 981–1191.

8. T. J. Gravestock, M. A. Blitz, W. J. Bloss and D. E. Heard, ChemPhysChem, 2010, **11**, 3928−3941.